Microbunching Instability due to Bunch Compression

Zhirong Huang, Juhao Wu (SLAC)
Timur Shaftan (BNL)
mail to: zrh@slac.stanford.edu

1   Introduction

Magnetic bunch compressors are designed to increase the peak current while maintaining the transverse and longitudinal emittances in order to drive a short-wavelength free electron laser (FEL). Recently, several linac-based FEL experiments observe self-developing micro-structures in the longitudinal phase space of electron bunches undergoing strong compression [1-3]. In the mean time, computer simulations of coherent synchrotron radiation (CSR) effects in bunch compressors illustrate that a CSR-driven microbunching instability may significantly amplify small longitudinal density and energy modulations and hence degrade the beam quality [4]. Various theoretical models have since been developed to describe this instability [5-8]. It is also pointed out that the microbunching instability may be driven strongly by the longitudinal space charge (LSC) field [9,10] and by the linac wakefield [11] in the accelerator, leading to a very large overall gain of a two-stage compression system such as found in the Linac Coherent Light Source (LCLS) [12].

This paper reviews theory and simulations of microbunching instability due to bunch compression, the proposed method to suppress its effects for short-wavelength FELs, and experimental characterizations of beam modulations in linear accelerators. A related topic of interests is microbunching instability in storage rings, which has been reported in the previous ICFA beam dynamics newsletter No. 35 (http://www-bd.fnal.gov/icfabd/Newsletter35.pdf).

2   Sources of initial beam modulations

The high-brightness electron beams required for a short-wavelength FEL are generated by photocathode rf guns. Electron density modulations will be produced during the photoemission process since the typical drive laser intensity profile is not smooth. In fact, the laser intensity modulation may even be enhanced when a flat-top temporal distribution is desired to mitigate the space charge induced emittance growth, as demonstrated by recent experimental studies of temporal pulse shaping techniques [13]. The initial bunch current spectrum may be characterized by a bunching factor

$$b_0(k_0) = \frac{1}{Nec} \int I_0(z_0)e^{-ik_0z_0}dz_0 \; , \qquad (1)$$

where $I_0(z_0)$ is the initial current profile as a function of the longitudinal position z_0 (with the bunch head at $z_0 > 0$), $\lambda_0 = 2\pi/k_0$ is the initial modulation wavelength under considerations, and N is the total number of electrons. At relatively low beam energies in the gun section, the electrons repel each other in the higher density regions and initiate the space charge oscillation between density and energy modulations. The initial density modulation may be reduced at the expense of the increased energy modulation. This process will be further discussed in Sec. 4.1.

In addition to any residual density and energy modulations created by the non-smooth laser profile, the electron density modulation can be caused by shot noise fluctuations as well. Since the gain bandwidth of the microbunching instability is very broad as discussed below, the shot noise bunching is on the order of $1/\sqrt{N_\lambda}$, where N_λ is the number of electrons per modulation wavelength.

3 Theory

3.1 Gain mechanism

The mechanism for microbunching instability is similar to that in a klystron amplifier [9,5]. A high-brightness electron beam with a small amount of density modulation can create longitudinal self-fields that lead to beam energy modulation. Since a magnetic bunch compressor (usually a chicane) introduces path length dependence on energy, the induced energy modulation is then converted to additional density modulation that can be much larger than the initial density modulation. This amplification process (the gain in microbunching) is accompanied by a growth of energy modulation and a possible growth of emittance if significant energy modulation is induced in a dispersive region such as the chicane. Thus, the instability can be harmful to short-wavelength FEL performance by degrading the beam quality.
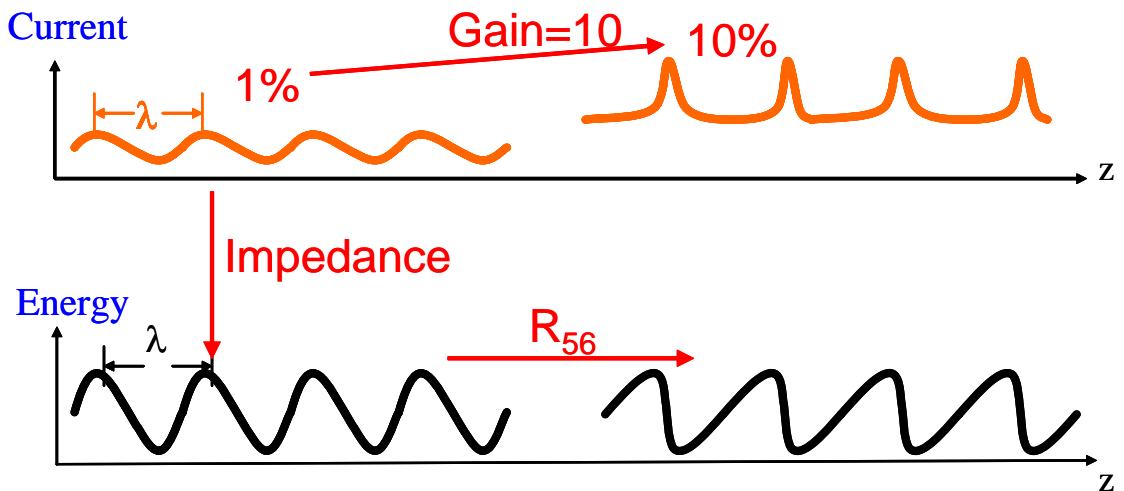
Figure 1: An illustration of microbunching instability in a bunch compressor.

It is typical to assume that modulation wavelengths are much shorter than the electron bunch length, and that density modulation amplitudes are much smaller than the average current. Under these assumptions, the amplitude of the density modulation at each wavelength grows independently and is characterized by a gain spectrum $G(k_0)$ of the accelerator system:

$$G(k_0) = \left| \frac{b_f(k_f)}{b_0(k_0)} \right| \ , \tag{2}$$

where $b_f(k_f)$ is the final bunching factor for the compressed wavenumber k_f corresponding to k_0.

In what follows, we further divide the self-fields into two categories: the self-fields created upstream of the bunch compressors such as the LSC field and linac wakefields, and the self-fields created during the compression process such as CSR. Although the gain mechanism is the same for all impedance sources, the treatment of CSR instability is more complicated due to the coupling of transverse and longitudinal motions in a bunch compressor.

3.2   Microbunching gain due to LSC and wakfields upstream of the compressor

Any wakefield upstream of a bunch compressor can contribute to beam energy modulation. For very short modulation wavelengths under considerations, we can neglect effects of vacuum chamber and use the free-space LSC impedance per unit length (see, e.g., Ref. [14,15])

$$Z_{LSC}(k_0) = \frac{iZ_0}{\pi k_0 r_b^2} \left[1 - \frac{k_0 r_b}{\gamma} K_1\left(\frac{k_0 r_b}{\gamma} \right) \right] \approx \frac{iZ_0 k_0}{4\pi\gamma^2} \left(1 + 2\ln\frac{\gamma}{k_0 r_b} \right) \ , \ \text{when} \ \frac{k_0 r_b}{\gamma} << 1 \ , \tag{3}$$

where $Z_0 = 377 \ \Omega$ is the free space impedance, r_b is the beam radius of a uniform cross section, and K_1 is the modified Bessel function. The high-frequency behaviour of the geometric impedance in a periodic accelerating structure is [16]

$$Z_{Linac}(k_0) = \frac{iZ_0}{\pi k_0 a^2} \ , \tag{4}$$

where a is the average iris radius of the accelerating structure. Note that both LSC and the high-frequency linac impedance are imaginary, indicating redistribution of beam energy without any net energy loss. The LSC impedance is the dominant contribution to the microbunching instability at very high frequencies when $ka/\gamma >> 1$ [10].

At about 100 MeV or higher beam energies, the electron density modulation is basically frozen in the linac, and the energy modulation accumulates according to

$$\Delta\gamma_m(k_0) = -\frac{I_0 b_0(k_0)}{I_A} \int_0^L ds \frac{4\pi Z(k_0;s)}{Z_0} \ , \tag{5}$$

where $I_A \approx 17$ kA is the Alfven current, $Z = Z_{LSC} + Z_{Linac}$ is the total impedance, and s is the bunch position along the accelerator beam line, and L is the total length of the linac.

The accumulated energy modulation is then converted to additional density modulation by a bunch compressor with the momentum compaction R_{56}. For a gaussian energy distribution with the intrinsic rms energy spread $\sigma_\delta = \sigma_\gamma/\gamma_b$ prior to the bunch

compressor (at energy $\gamma_b mc^2$), the gain in density modulation after the compressor is [9]

$$G \approx \frac{I_0}{\gamma_b I_A} \left| k_f R_{56} \int_0^L ds \frac{4\pi Z(k_0;s)}{Z_0} \right| \exp\left(-\frac{k_f^2 R_{56}^2 \sigma_\delta^2}{2} \right) . \qquad (6)$$

Here $k_f = k_0 /(1+hR_{56})$ is the compressed modulation wavenumber, and $h<0$ is the linear energy chirp in front of the compressor (relative energy correlation divided by the bunch length). The gain typically peaks when $k_f R_{56} \sigma_\delta \approx 1$, and is exponentially suppressed at shorter modulation wavelengths. Since the LSC impedance scales almost linearly with k_0, the maximum LSC-induced microbunching gain scales as $\sigma_\delta^{-2} R_{56}^{-1}$ and depends sensitively on the intrinsic energy spread.

3.3 Microbunching gain due to CSR in a compressor chicane

The electron density modulation is a source of CSR emission in a bunch compressor chicane. The resulting energy modulation due to the CSR force in one dipole can be converted into additional density modulation at the next dipole, giving rise to the CSR instability inside a bunch compressor. For modulation wavelengths much shorter than the electron bunch length, we can neglect shielding effects of conducting walls and transient effects associated with short bends to employ the longitudinal CSR impedance for a line charge model [17,18]:

$$Z_{CSR}(k;s) = (1.63+0.94i)\frac{Z_0 k^{1/3}}{4\pi\rho(s)^{2/3}} , \qquad (7)$$

where $\rho(s)$ is the bending radius at a distance s from the beginning of the bunching compressor. The Effective longitudinal CSR force for a bunch with the finite transverse extend is discussed in Ref. [19,20].

However, the density modulation is no longer frozen in the chicane. In fact, the longitudinal motion in a dipole is coupled to the horizontal motion, and the density modulation is subject to emittance damping when the path length spread due to a finite beam size is comparable to the reduced modulation wavelength [5], i.e.,

$$\frac{L_d}{\rho}\sqrt{\varepsilon_0 \beta_0} \approx \frac{\lambda}{2\pi} . \qquad (8)$$

Here L_d is the length of the dipole, β_0 is the initial beta function, and ε_0 is the transverse emittance. Taking into account the emittance effect and changes of modulation wavelengths due to compression, the CSR microbunching is governed by an integral equation as [6,7]

$$b(k(s);s) = b_0(k(s);s) + \int_0^s d\tau K(\tau,s)b(k(\tau);\tau) , \qquad (9)$$

where the kernel is

$$K(\tau,s) = ik(s)R_{56}(\tau \to s)\frac{I(\tau)Z_{CSR}(k(\tau);\tau)}{\gamma_b I_A}\exp\left[-\frac{k_0^2 U^2(s,\tau)\sigma_\delta^2}{2}\right]$$

$$\times \exp\left[-\frac{k_0^2 \varepsilon_0 \beta_0}{2}\left(V(s,\tau) - \frac{\alpha_0}{\beta_0} W(s,\tau)\right)^2 - \frac{k_0^2 \varepsilon_0}{2\beta_0} W^2(s,\tau)\right], \quad (10)$$

$k(\tau)/B(\tau) = k(s)/B(s) = k_0$, $B(s) = (1 + hR_{56}(s))^{-1}$, $I(\tau) = I_0 B(\tau)$ is the peak current at the location τ, α_0 is the initial Twiss parameter, and

$$U(s,\tau) = B(s)R_{56}(s) - B(\tau)R_{56}(\tau),$$
$$V(s,\tau) = B(s)R_{51}(s) - B(\tau)R_{51}(\tau),$$
$$W(s,\tau) = B(s)R_{52}(s) - B(\tau)R_{52}(\tau). \quad (11)$$

For typical four-dipole chicanes, the integral equation can be solved by an iterative method to obtain analytical formulas for the final gain [7]. The results are compared to two numerical tracking codes (*ELEGANT* [21] and CSR_calc [22]) for a benchmark chicane (see http://www.desy.de/csr/ for more details) as shown in Figure 2 [23].
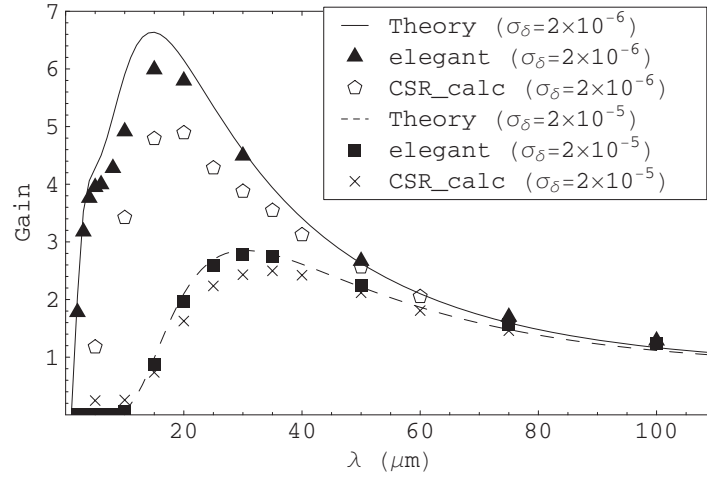
Figure 2: CSR microbunching gain for a benchmark chicane as a function of the initial modulation wavelength for $\gamma\varepsilon_0 = 1\ \mu$m at 5 GeV.

3.4   Landau damping with a laser heater

When more than one bunch compressors are present in the accelerator, the overall gain is the product of individual compressor gains that includes LSC, CSR and linac wakefield effects. For the very small uncorrelated energy spread generated from a photocathode rf gun (with a measured rms value of 3 to 4 keV [24]), the peak overall gain can be very large (>1000) for a two-stage compression system found in typical x-ray FEL designs and can even significantly amplify the electron shot noise. The gain is usually dominated by the LSC effect as the CSR microbunching is subject to emittance damping discussed above. Thus, the only effective way to suppress the large gain is to increase the uncorrelated energy spread before compressing the bunch. Ref. [10] suggests a laser heater that makes use of resonant laser-electron interaction in a short undulator to induce rapid energy modulation at the optical frequency as an effective energy spread for Landau damping. For an undulator with a strength parameter K and a length of L_u, the amplitude of the energy modulation at the resonant laser wavelength is

$$\Delta\gamma_L = \sqrt{\frac{P_L}{P_0}}\frac{KL_u}{\gamma_0\sigma_r}\left[\mathrm{J}_0\left(\frac{K^2}{4+2K^2}\right)-\mathrm{J}_1\left(\frac{K^2}{4+2K^2}\right)\right]\exp(-\frac{r^2}{4\sigma_r^2})\ ,\qquad (12)$$

where P_L is the laser peak power, $P_0 \approx 8.7$ GW, J_0 and J_1 are the usual Bessel functions associated with a planar undulator, and σ_r is the rms laser spot size in the undulator.

For the LCLS x-ray FEL operated at the radiation wavelength of 1.5 Å, the uncorrelated rms energy spread can be increased from about 3 keV produced by the rf gun to about 40 keV without degrading the FEL performance. The LCLS laser heater is designed in a small magnetic chicane near the end of the photoinjector at 135 MeV as shown in Fig. 3 [12], with a total undulator length of about 0.5 m. The laser rms spot size is chosen to match the electron rms transverse beam size in order to generate a more Gaussian-like energy profile for effective Landau damping. The modest amount of the laser power ($P_L \approx 1$ MW) is provided by the 800-nm Ti:sapphire laser that drives the photocathode rf gun. In addition to easy optical access, the chicane provides a useful temporal washing effect (due to transverse and longitudinal coupling) that completely smears the laser-induced 800 nm energy modulation. The induced emittance growth due to the energy change in the chicane is negligible. The overall microbunching gain can be reduced to a tolerable level determined by beam dynamics simulations to be discussed next. A similar laser heater has also been adopted by the FERMI FEL project at Trieste [25].
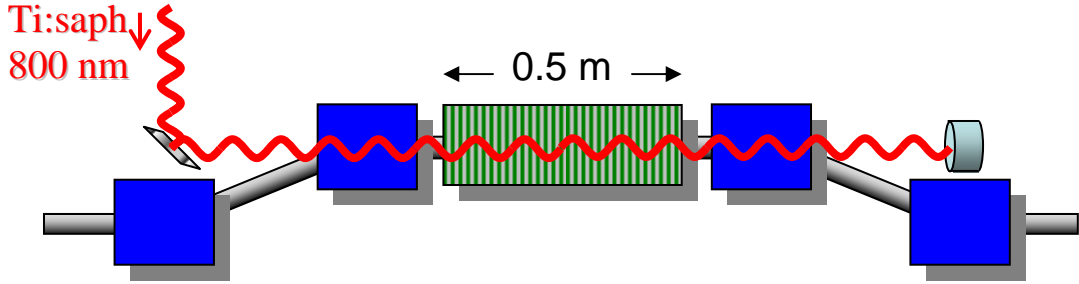
Figure 3: Layout of the LCLS laser heater inside a magnetic chicane at the injector end ($\gamma_0 mc^2 = 135$ MeV).

4 Simulations

The detrimental effects of microbunching instability in bunch compressors are first illustrated by computer simulations [4]. Since the modulation wavelengths are generally small compared to the electron bunch length, the simulations require a longitudinal bin size much smaller than the wavelength and hence typically use a million or more macroparticles. Even with the use of quiet loading algorithms such as the Halton sequence, numerical noise remains an issue in start-to-end simulations and must be controlled to an acceptable level. We discuss some of these issues here and the start-to-end LCLS simulations that demonstrate the function of the laser heater and set the tolerable drive laser modulation amplitudes.

4.1   Injector simulations

As mentioned in Sec. 2, LSC can not be described by a simple impedance element at the low energy injector region due to space charge oscillation dynamics. Such an oscillation will convert density modulation into energy modulation and vice versa. For a relativistic beam in a drift space, we can estimate the space charge oscillation frequency as [14,15]

$$\omega_{sc} = c\left[\frac{I_0}{\gamma^3 I_A} k_0 \frac{4\pi |Z_{LSC}(k_0)|}{Z_0}\right]^{1/2} \leq \frac{2c}{r_b}\left(\frac{I_0}{\gamma^3 I_A}\right)^{1/2} \equiv \omega_p, \qquad (13)$$

where ω_p is the plasma frequency. For example, if $r_b = 200$ μm, $I_0 = 100$ A, and the modulation wavelength $\lambda_0 \in [50, 300]$ μm, the space charge oscillation distance is about 1.5 to 3.5 m for a 10 MeV beam, and increases to 10 to 45 m for a *30* MeV beam. Thus, space charge oscillation can be important at lower beam energies but becomes insignificant at higher energies for a given beam line. The space charge oscillation dynamics taking into account the transverse beam profile is analyzed recently in Refs. [26,27], and the effect of acceleration can be included by generalizing the integral equation for the CSR microbunching described above [28,27].

Nevertheless, full space charge simulations using *PARMELA* [29] or *ASTRA* [30] (including both longitudinal and transverse effects) are necessary to quantify the evolution of the electron density and energy modulations in the injector region. Both *PARMELA* and *ASTRA* space-charge simulations of the LCLS photoinjector show that the initial density modulation caused by the drive laser is only reduced by a factor of a few (3-6) at the end of the injector for a wide spectral range (from 25 μm to 300 μm), while noticeable energy modulation is accumulated [28]. The modulated beams after the injector simulation can then be used by *ELEGANT* for the main linac simulation. Note that much stronger damping of the initial density modulation in the TESLA Test Facility injector simulations has been reported in Ref. [31], although the origin of the damping mechanism is not well-understood.

4.2   Linac simulations

ELEGANT supplies two beamline elements that simulate the longitudinal CSR effect. One is a drift element and the other is a bending magnet. The CSR model used by *ELEGANT* is based on the energy change of an arbitrary line-charge distribution as a function of the bunch position in a dipole magnet [17,18], together with the proper treatment of transient effects including the drift space [32,33]. The CSR-induced energy change in both magnet and drift space is implemented in a kick-transport-kick algorithm. More details about how to split the magnets and how to choose the canonical integrator are discussed in Ref. [34]. One difficulty in these computations comes from noise in the linear density histogram due to the use of a finite number of particles and a large number of bins. This is a particular problem when taking derivative of the line density. Smoothing, e.g., Savitzky-Golay smoothing filter, is used to overcome this problem, at the expense of some loss of information. Therefore, it is necessary to vary both the number of particles and the amount of smoothing until numerical convergence is obtained in the simulations.

ELEGANT supplies two similar beamline elements for the LSC effect. One is a drift

element and the other is an rf cavity that also includes structure wakefields. The 1-D LSC impedance of Eq. (3) is used in a kick-drift-kick (or kick-accelerate-kick) algorithm. The distance l between kicks must be set properly to get a valid result. Normally, one sets $l << c/\omega_p$. The drift element automatically selects the drift distance, using $l = 0.1c/\omega_p$. The acceleration element requires the user to specify the number of parts to split the cavity into, and simply checks that $l \leq 0.1c/\omega_p$. For the case with acceleration, $l \leq 0.1\gamma/(d\gamma/ds)$ ensures that the momentum does not change too much between kicks. For a Gaussian or a parabolic transverse beam distribution, the effective beam radius is fitted as $r_b \approx 1.7(\sigma_x+\sigma_y)/2$ in Eq. (3), where σ_x and σ_y are the rms beam sizes in the transverse planes. Fast Fourier transformation (FFT) of the current histogram is then taken. A low-pass filter is normally used to control the high-frequency noise. The cutoff frequency and slope of the filter are specified by users. Generally, the number of bins is chosen such that the frequencies of interest are less than $0.2 F_n$, where F_n is the Nyquist frequency. The low-pass filter is then set to remove frequencies above $0.4 F_n$. The (filtered or unfiltered) FFT of the current is then multiplied by the impedance, and the result is inversely Fourier transformed. This gives the voltage as a function of bin in the original current histogram. This voltage can be applied to each particle, with interpolation between bins to make a smoother result. The LSC-induced energy modulations in *ELEGANT* are compared to *ASTRA* simulations and analytical results (i.e., Eq. (5)) as shown in Fig. 4 [12].
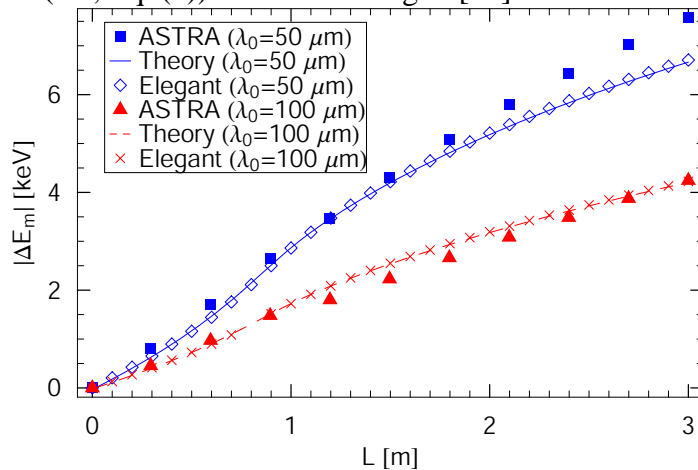
Figure 4: LSC-induced energy modulation amplitude as a function of the drift distance L for a 120-MeV, 120-A beam with a ±5% initial density modulation at 50 μm and 100 μm modulation wavelengths.

4.3 Discussion of simulation results

To illustrate how the microbunching instability may degrade the beam qualities, and to demonstrate the function of the laser-heater in suppressing the instability, Fig. 5 shows a typical longitudinal phase space comparison at the end of the LCLS accelerator with and without the laser-heater for an initial ±8% laser intensity modulation at $\lambda_0 = 150$ μm [35]. The start-to-end simulations are carried out by *ASTRA* for the injector and *ELEGANT* for the linac, with a separate tracking code for the resonant laser-electron interaction to simulate the heating process prior to the *ELEGANT* runs. Without the

laser heater, the very large final energy modulation (with the compressed wavelength of about 3 μm) due to the microbunching instability becomes effective slice energy spread for the FEL. As shown on the left plot of Fig. 6, such a large slice energy spread will degrade the FEL gain. The laser heater clearly limits the instability gain as well as the final slice rms relative energy spread to about 1.0×10^{-4}, which has a negligible effect on the LCLS performance. In the absence of the laser heater, the significant energy modulation induced by CSR in dipoles can couple to the growth of the slice horizontal emittance and further affect the FEL operation, while the slice emittance is entirely unaffected when the laser heater is on (see the right plot of Fig. 6). Similar conclusions can be made for other modulation wavelengths.

In fact, even though the high-frequency gain is significantly suppressed by the increased energy spread due to the laser heater, there are residual modulations at longer wavelengths, which are still visible on the right side of Fig. 5. This sets the initial tolerable density modulation amplitude to be about $\pm8\%$ at 150 μm. Since the gain is broad and is relatively insensitive to initial wavelengths between 50 μm to 300 μm, the maximum laser intensity modulation amplitude at the cathode is determined to be about 5% (rms) in order for the laser-heater suppressed microbunching to not affect the LCLS FEL [35].
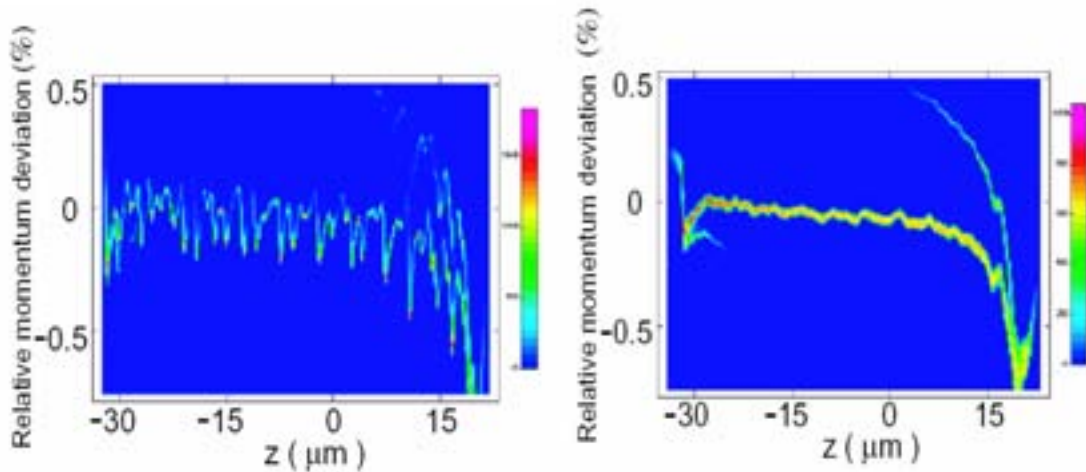
Figure 5: Longitudinal phase space distribution at the entrance of the LCLS undulator for an initial $\pm8\%$ laser intensity modulation at $\lambda_0 = 150$ μm in the start-to-end simulation without the laser-heater (left plot) and with the laser heater (right plot).
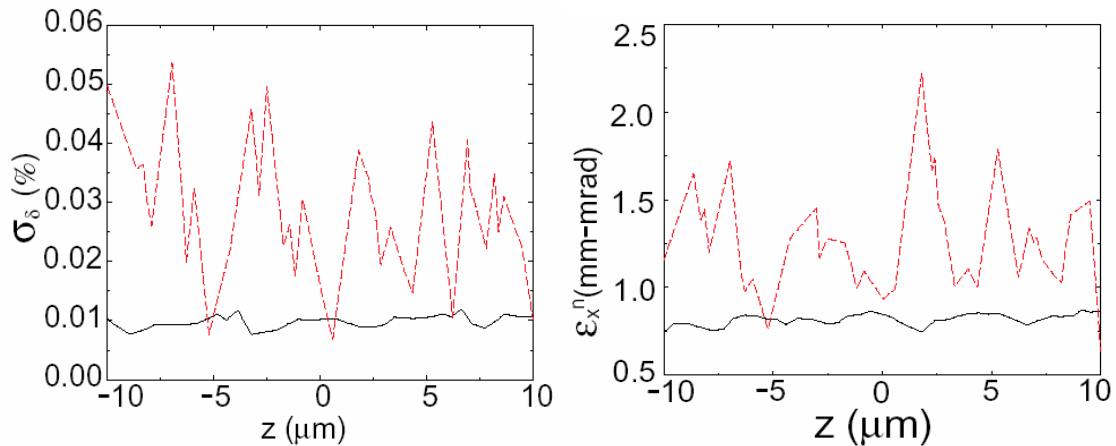
Figure 6: Slice rms relative energy spread σ_δ (left plot) and slice normalized emittance

ε_x^n (right plot) at the entrance of the LCLS undulator for an initial ±8% laser intensity modulation at $\lambda_0 = 150$ μm in the start-to-end simulation. Solid curve stands for the result with the laser-heater; and dashed curve for the result without the laser-heater.

5   Experimental observations and analyses

Due to the extremely short time scales associated with compressed bunches, longitudinal phase space characterizations usually rely on measurements of chirped beam energy spectra. Up to date quite a few linac-based FEL facilities report a self-developing microstructure when the bunch undergoes strong compression [1-3].

In energy-recovery accelerators the microstructure is observed at Jefferson Lab IR-demo FEL during compression experiments [1]. While approaching the maximum compression the bunch energy profile started to show a fine structure; such effect is systematically enhanced as the charge per bunch is increased.

More recently strong break-up of energy spectrum near the phase of maximum compression is observed at the Accelerator Test Facility (BNL) [36]. Currently this effect is being studied experimentally and in simulations.

At the commissioning stage of Deep Ultraviolet FEL (DUV-FEL at NSLS, BNL) and TESLA Test Facility (TTF-1 at DESY), strong modulations of the chirped bunch energy spectra are observed and analyzed [2,3] (see Fig. 7). The chirp (or the linearly correlated energy spread) is provided by running one of the accelerating sections off the crest of the accelerating voltage. The local brightness in the image is linearly proportional to the local amount of charge. The horizontal coordinate of the beam image scales with energy; the position of the image centroid is defined by the average beam energy. Electrons, located in the head (tail) of the bunch, gain (lose) energy while traveling through the accelerator section, but the energy of the beam centroid stays constant. Therefore the bunch gets dispersed along the horizontal axis of the monitor and the head (tail) of the bunch gets mapped on the right (left) side of the monitor screen. This setup is a particular implementation of the so-called ''zero-phasing'' method of bunch length measurement [37].
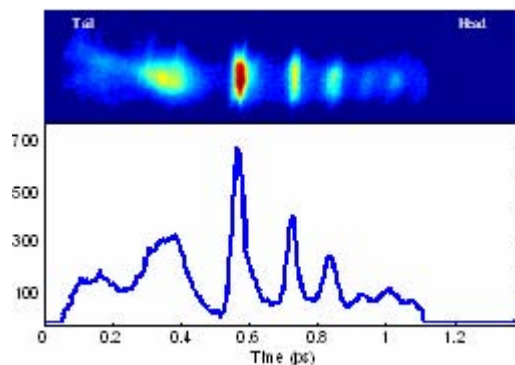
Figure 7: Example of the beam energy spectrum measurement at the DUV-FEL (BNL). Modulated beam image after spectrometer (upper plot), vertical axes is Y-coordinate; horizontal one is proportional to the beam energy. Bottom figure: "zero-phasing" projection of the beam on upper plot, horizontal axis is scaled in picoseconds.

The experiments at TTF include changes of the compressor strength by varying the amount of energy chirp, variation of charge per bunch and tomographic reconstruction of the longitudinal phase space [38]. The measurements show that the structure appears only when the beam is compressed; at the same time the chicane itself does not impose any structure when the beam passes the chicane without energy chirp.

At the TTF among the different sources of wakefields a possible mechanism based on the CSR self-interaction in the bunch compressor is considered [39]. Calculations with TraFiC[4] code [40] indicate that the CSR force has the strength to yield the energy redistribution similar to the measurements. It is shown that, if non-linearities such as the curvature of the accelerating RF sections are significant, compression would produce non-Gaussian and locally peaked distributions. For such types of distributions, CSR effects can be much stronger compared to Gaussian distributions with the same rms bunch lengthes. The LSC microbunching instability is also considered as a possible candidate for the strong distortions of longitudinal phase space [9].

Another way of interpreting sharp spikes in the energy spectrum is discussed in Ref. [15]. After strong compression significant beam energy modulation may be induced during the off-crest acceleration before the energy spectrometer for a small initial density modulation,. The projection of this energy-modulated phase space onto energy axis (chirped energy spectrum) can exhibit sharp spikes similar to that observed in the experiments (see Fig. 8).
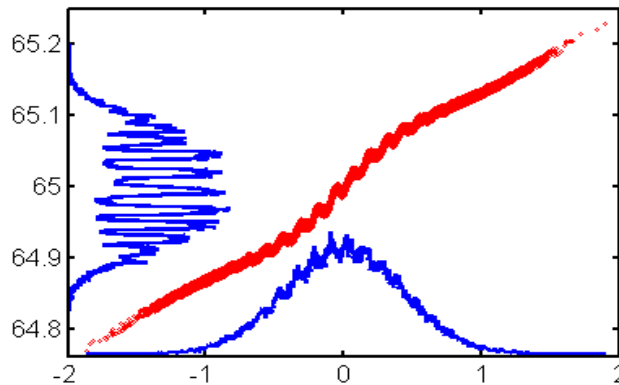
Figure 8: Illustration of electron bunch longitudinal phase space. Abscissa is time (ps), ordinate is energy (MeV). Beam energy modulation along the chirped bunch leads to deeply modulated energy spectra.

To determine whether the energy modulation or the density bunching dominates the observed structure (such as in Fig. 7), two additional experiments are performed at the DUV FEL [41].

The goal of the first experiment is to study the sensitivity of the modulation to beam size changes along the zero-phasing section of the accelerator after the bunch compressor. Adjusting quadrupoles in the transport line after the chicane, three focusing solutions are established and provide three different beam envelopes (0.25, 0.5, 1.0 mm average rms beam size along the transport line). It is explicitly shown that the strong modulation, present when the beam size is small, almost vanishes at a larger beam cross section. The observed structure, if caused by strong density modulations, should not be very sensitive to changes in transverse beam dimensions after compression. On the contrary, LSC-induced energy modulations in the linac can have a strong dependence on the beam size for the DUV-FEL parameters.

In the next experiment CTR power is measured from electron bunches with drastically different modulation amplitudes (given by different beam sizes along the zero-phasing section) under the same experimental conditions. Measured values of power for various CTR wavelength ranges do not differ for the two cases, indicating that the spectral content of density modulation is the same in both cases. These experiments confirm that the observed structure is dominated by energy modulation instead of current modulation.

To determine the range of modulation frequencies and amplitudes, another experiment is performed [42]. This time the energy of the bunch is varied, and a set of "zero-phasing" images are recorded. Initial analysis of the results shows major difference in frequency and amplitude content of the structure at different energies. For instance, the number of spikes (and the modulation wavelength) in a "zero-phasing" image is found linearly proportional to the beam energy. The modulation amplitude increases as the beam energy is decreased, in general agreement with the energy dependence of the LSC impedance discussed in Sec. 3.2. The experimental data are then processed and dependences of the modulation wavelength and amplitude are compared with the analytic calculation and simulations, yielding a reasonable agreement (see Fig. 9). The numerical simulations, implemented in *MATLAB* [42], use the same LSC computation algorithm as described in 1.1.4.2.
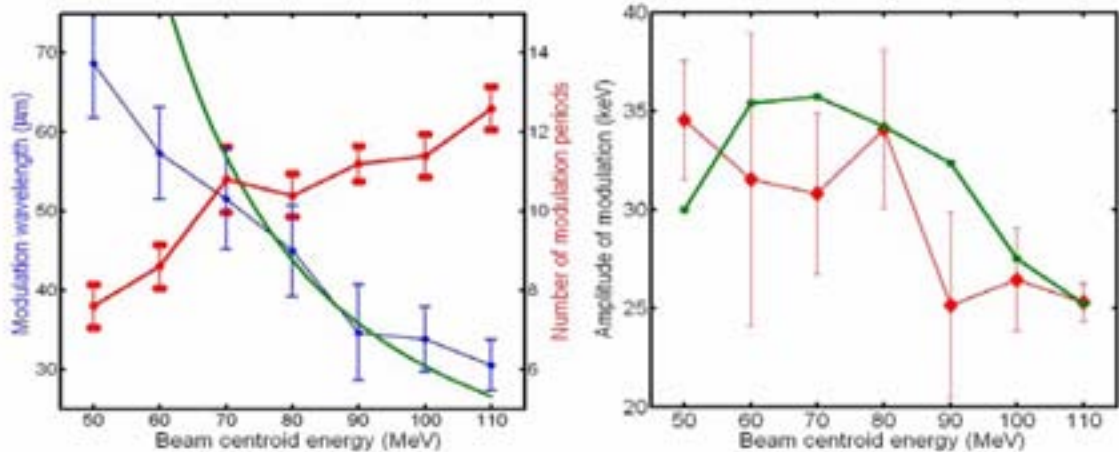
Figure 9: Dependence of modulation wavelength (left plot) and modulation amplitude (right plot) on energy. Red and blue traces correspond to the measured data; green traces correspond to analytic calculation (left plot) and simulation result (right plot).

Note that the observed amplitude of final energy modulation is in the range of 20–40 keV, which exceeds the expected intrinsic energy spread (less than 10 keV for this experiment) by a large factor. Simulations also demonstrate that reconstructed amplitudes of energy modulation (Fig. 10) correspond to about 3% of initial density modulations [42], comparable with the measured intensity fluctuations of the DUV-FEL rf gun drive laser pulse. Thus, nonuniformities in the longitudinal density profile in the range of only a few percent can cause strong energy modulations due to the action of the space charge force.
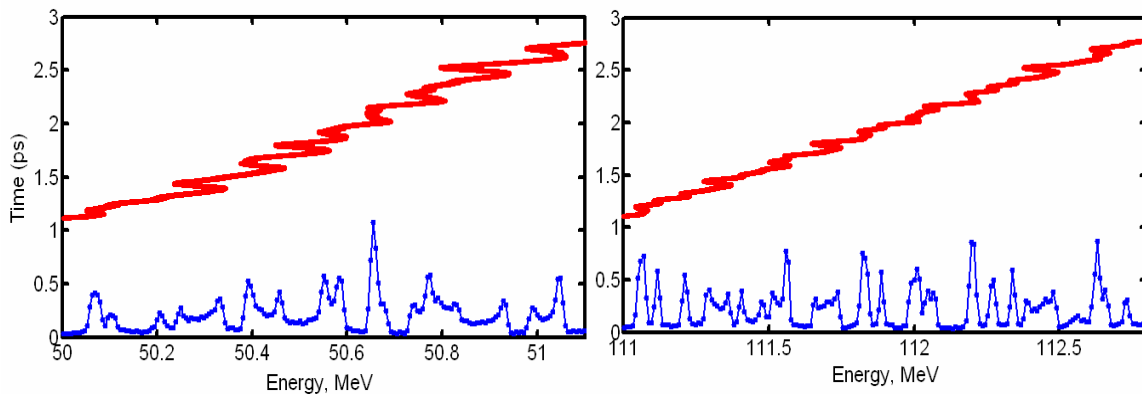
Figure 10: Simulated phase space at the end of the accelerator for two different energies (50 and 110 MeV).

In the DUV-FEL accelerator the strong energy modulation occurs while a beam with a modest peak current (~200 A) travels along the accelerator of only 15 m. For much longer accelerators with two-stages of compression such as proposed for short-wavelength FELs, this effect can be much stronger and can lead to a significant microbunching instability that degrades the electron beam quality beyond the FEL tolerance. Therefore, these experimental results and their analysis warrant controlled increase of the intrinsic energy spread by a laser heater to suppress the microbunching instability.

6   Acknowledgments

7   References

1. Ph. Piot et al., in Proc. of EPAC2000, 1546 (2000).
2. W. Graves et al., in Proc. of PAC2001, 2224 (2001).
3. M. Hüning, Ph. Piot and H. Schlarb, Nucl. Instrum. Meth. A **475**, 348 (2001).
4. M. Borland et al., in Proc. of PAC2001, 2707 (2001); Nucl. Instrum. Meth. A **483**, 268 (2002).
5. E. Saldin, E. Schneidmiller, and M. Yurkov, Nucl. Instrum. Meth. A **490**, 1 (2002).
6. S. Heifets, G. Stupakov, and S. Krinsky, Phys. Rev. ST Accel. Beams **5**, 064401 (2002); 129902 (2002).
7. Z. Huang and K.-J. Kim, Phys. Rev. ST Accel. Beams **5**, 074401 (2002); 129903 (2002).
8. S. Reiche and J. B. Rosenzweig, Phys. Rev. ST Accel. Beams **6**, 040702 (2003).
9. E. Saldin, E. Schneidmiller, and M. Yurkov, Nucl. Instrum. Meth. A **483**, 516 (2002).
10. E. Saldin, E. Schneidmiller, and M. Yurkov, Nucl. Instrum. Meth. A **528**, 355 (2004).
11. Z. Huang et al., in Proc. of PAC2003, 3140 (2003).

12. Z. Huang et al., Phys. Rev. ST Accel. Beams **7**, 074401 (2004).
13. H. Loos et al., in Proc. of PAC2005, 642 (2005).
14. J. Rosenzweig et al., DESY TESLA-FEL-96-15 (1996).
15. Z. Huang and T. Shaftan, Nucl. Instrum. Meth. A **528**, 345 (2004)
16. R. Gluckstern, Phys. Rev. D **39**, 2780 (1989).
17. J. Murphy, S. Krinsky, and R. Gluckstern, in Proc. of PAC1995, 2980 (1995).
18. Y. Derbenev et al., DESY TESLA-FEL-95-05 (1995).
19. M. Dohlus, presented at *The CSR workshop*, Zeuthen, Germany, 2002 (http://www.desy.de/csr/).
20. R. Li, JLAB-TN-05-046 (2005).
21. M. Borland, ANL Advanced Photon Source Report No. LS-287 (2000).
22. P. Emma, CSR_calc code.
23. Z. Huang et al., Nucl. Instrum. Meth. A **507**, 318 (2003).
24. M. Hüning and H. Schlarb, in Proc. Of PAC2003, 2074 (2003).
25. S. Di Mitri et al., in Proc. of FEL2005 (2005).
26. G. Geloni et al., Nucl. Instrum. Meth. A **554**, 20 (2005).
27. J. Wu, Z. Huang, and P. Emma, SLAC-PUB-11448, in Proc. of FEL2005 (2005).
28. C. Limborg et al., in Proc. of EPAC2004, 1506 (2004).
29. L.Young and J.Billen , PARMELA code.
30. K.Floettmann, ASTRA code (https://www.desy.de/~mpyflo/).
31. Y.-J. Kim, D. Son, Y. Kim, Nucl. Instrum. Meth. A **528**, 427 (2004).
32. E. Saldin, E. Schneidmiller, and M. Yurkov, Nucl. Instrum. Meth. A **398**, 373 (1997).
33. G. Stupakov and P. Emma, in Proc. of EPAC2002, 1479 (2002).
34. M. Borland, Phys. Rev. ST Accel. Beams **4**, 070701 (2001).
35. J. Wu et al., in Proc. of LINAC2004, 390 (2004).
36. G. Andonian, presented at *The Physics and Applications of High Brightness Electron Beams,* Erice, Italy, 2005 (http://www.physics.ucla.edu/PAHBEB2005/talks/10_oct_2005/wg_2/g_andonian.pdf).
37. D. Wang, G. Krafft, and C. Sinclair, Phys. Rev. E **57**, 2283 (1998).
38. M. Hüning, in Proc. of DIPAC2001, 56 (2001).
39. T. Limberg, Ph. Piot, and E.A. Schneidmiller, Nucl. Instrum. Meth. A **475**, 353 (2001).
40. M. Dohlus, A. Kabel, and T. Limborg, Nucl. Instrum. Meth. A **445**, 338 (2000).
41. T. Shaftan et al., Nucl. Instrum. Meth. A **528**, 397 (2004).
42. T. Shaftan and Z. Huang, Phys. Rev. ST Accel. Beams **7**, 080702 (2004).